Applied Surface Science 643 (2024) 158725

Contents lists available at ScienceDirect

Applied Surface Science

journal homepage: www.elsevier.com/locate/apsusc

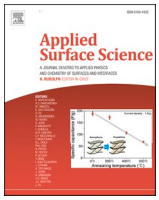

Full Length Article

Encapsulation of $Cs_3Bi_2Br_9$ perovskite photocatalyst with polythiophene for prolonged activity in oxidizing and humid environment

Magdalena Miodyńska [a,*], Olga Kaczmarczyk [b], Wojciech Lisowski [c], Andrzej Żak [b], Tomasz Klimczuk [d], Monika Paszkiewicz [e], Adriana Zaleska-Medynska [a,*]

[a] Department of Environmental Technology, Faculty of Chemistry, University of Gdansk, 80-308 Gdansk, Poland
[b] Institute of Advanced Materials, Faculty of Chemistry, Wroclaw University of Science and Technology, 50-370 Wroclaw, Poland
[c] Institute of Physical Chemistry, Polish Academy of Science, 01-224 Warsaw, Poland
[d] Faculty of Applied Physics and Mathematics and Advanced Materials Center, Gdansk University of Technology, 80-233 Gdansk, Poland
[e] Department of Environmental Analysis, Faculty of Chemistry, University of Gdansk, 80-308 Gdansk, Poland

ARTICLE INFO

Keywords:
Photocatalysis
Bi-based perovskite
Lead-free perovskite
Halide perovskite
Ex-situ transmission electron microscopy

ABSTRACT

Despite their growing popularity in modern technology, halide perovskites suffer from susceptibility to oxidation, limiting their applications. Our aim was to enhance $Cs_3Bi_2Br_9$ perovskite's performance in humid environments through polythiophene encapsulation. This extended its lifespan while preserving photocatalytic abilities, as demonstrated in toluene decomposition experiments. We confirmed the stability of $Cs_3Bi_2Br_9$ encapsulated with polythiophene over four photocatalytic cycles and identified photogenerated electrons and superoxide radicals as key contributors to toluene decomposition. Benzaldehyde was detected as the primary toluene decomposition product, and we observed partial pollutant mineralization, evidenced by increased CO_2 concentration after photocatalysis. Additionally, using hybrid ex–situ transmission electron microscopy, we observed delayed oxidation of encapsulated perovskite. Encapsulation hindered, but did not entirely prevent, water vapor penetration into $Cs_3Bi_2Br_9$ particles. This progress suggests promising prospects for perovskite–based composites retaining photocatalytic capabilities under elevated humidity conditions.

1. Introduction

Halide perovskites are very popular semiconductors because of their unique photophysical properties, such as high power conversion efficiency, high charge carrier mobility, high light absorption abilities, and small exciton binding energy [1–5]. Furthermore, each of these features drives the widespread potential application of this type of material in the fields of solar cells (PSCs- *Perovskite Solar Cells*) [6], photodetectors [7], bioimaging [8], lasing [9], light-emitting diodes [10], photocatalytic processes [11,12] and many others.

Nevertheless, there are several justified limitations regarding the use of this type of material [13,14]. One such limitation is the eco-environmental concern, which appears to have been addressed thus far. Typical halide perovskites of the $CsPbX_3$ type (where X represents Cl, Br, I, or a mixture) contain toxic lead ions within their structure. However, these cations have been successfully substituted with alternatives such as Sn or Bi [2,15], or a combination of two different cations (e.g., Ag and Bi) to form double halide perovskite structures [16]. On the other hand, a more significant limitation in the application of perovskites is their exceptionally high instability upon indirect exposure to moisture and oxygen and their sensitivity to light exposure [17]. Consequently, resolving this issue has proven to be a major challenge for a wide range of researchers thus far. To date, the literature has reported numerous possibilities for protecting the halide perovskite structure from degradation, such as encapsulation with another material. This approach not only prevents degradation but can also introduce new hybrid properties [18]. Various methods can be employed to coat perovskites with metal oxides [19–21], other semiconductors [22,23], metal-organic frameworks [24–26], and polymers [27–31].

Furthermore, in the field of process engineering involving photocatalytic reactions, new photoactive and stable materials are continuously being discovered. Therefore, conductive polymer–stabilized halide perovskites appear to have potential as suitable candidates. Most of the existing studies focus on the encapsulation of lead–based perovskites [32–35]. Researchers applied a polymer coating to $CsPbBr_9$ perovskite to augment its luminescent properties and enhance the

* Corresponding authors.
E-mail addresses: magdalena.miodynska@ug.edu.pl (M. Miodyńska), adriana.zaleska-medynska@ug.edu.pl (A. Zaleska-Medynska).

https://doi.org/10.1016/j.apsusc.2023.158725
Received 14 July 2023; Received in revised form 16 October 2023; Accepted 19 October 2023
Available online 20 October 2023

stability of the resultant systems in aqueous environments [32–34]. These modifications have proven advantageous for the utilization of polymer-modified perovskites in solar cell applications [35]. In our case, we aimed to develop hybrid materials with lower toxicity by utilizing a bismuth analog of perovskite, $Cs_3Bi_2Br_9$. Our previous work confirmed the decomposition of this material upon contact with water, resulting in the formation of BiOBr and the release of Cs ions into the environment [11]. Thus, we employed an in situ polymerization method to wrap $Cs_3Bi_2Br_9$ nanoparticles, which proved to be more effective in encapsulating these sensitive particles within the matrix. Additionally, in this study, we achieved three different thicknesses of the polythiophene layer on the perovskite surface for the first time. To evaluate the photoactivity and stability of the Pth/perovskite composite, both modified and pristine perovskites were tested in a photocatalytic degradation reaction using toluene as a model environmental pollutant. Our results clearly demonstrated the enhanced activity and stability of the perovskite when encapsulated with the conductive polymer. The characterization of the nanomaterials, including perovskites and their nanostructures, was supported by transmission electron microscopy (TEM) imaging, which is a commonly used technique for this issue. Through TEM imaging, we could monitor the morphology and structure changes of both bare and modified perovskite during temporary exposure to water vapor. Based on these observations, it can be concluded that encapsulating the perovskite with a polymer increases its stability over time during contact with water. To the best of our knowledge, such experiments have not been previously conducted for the polythiophene–$Cs_3Bi_2Br_9$ system.

2. Materials and methods

The following reagents were used for the preparation of $Cs_3Bi_2Br_9$ perovskite: $BiBr_3$ (≥98 %, Sigma-Aldrich), CsBr (99.999 %, Sigma-Aldrich), DMSO (analytical grade, ChemPur), OA (oleic acid, technical grade 90 %, Sigma-Aldrich), OLAm (oleylamine, ≥98 %, Sigma-Aldrich), anhydrous ethanol (99.8 vol%, POCH S.A.).

For the preparation of Pth/$Cs_3Bi_2Br_9$ samples, the following reagents were used: chloroform (analytical grade, ChemPur, Piekary Slaskie, Poland), thiophene (fluorochem, UK), $FeCl_3$ (97 %, Sigma-Aldrich) and methanol (analytical grade, STANLAB, Lublin, Poland). Anhydrous ethanol (99.8 vol%, POCH S.A.) and methanol (analytical grade, STANLAB, Lublin, Poland) were also used to purify the perovskite and Pth/$Cs_3Bi_2Br_9$ samples, respectively. The following reagents were used in the photocatalytic research: toluene (analytical grade, EUROCHEM BGD, Tarnow, Poland) as the model environmental pollutant, benzoquinone (BQ) (≥98 %, Sigma-Aldrich), $AgNO_3$ (analytical grade, STANLAB), ammonium oxalate (OA) (≥99 %, Sigma-Aldrich), tert–butanol (*t*-Bu) (≥99.3 %, Sigma-Aldrich), butylated hydroxytoluene (BHT) (≥99 %, Sigma-Aldrich). Powder X-ray diffraction experiments were performed at a temperature of 20 °C, employing powdered samples. The diffraction data were acquired using a Bruker D8 Focus diffractometer equipped with Cu Kα radiation (λ = 1.54 Å) and a LynxEye XE-T detector. The data collection range spanned from 10° to 60° 2θ, and the acquisition time was set at 30 min. To ascertain the crystal structure type and lattice parameters of the examined samples, LeBail refinement of the powder X-ray diffraction pattern was executed, utilizing HighScore Plus version 3.0e software. Diffuse reflectance spectra were acquired using a UV–Vis spectrophotometer (UV 2600, Shimadzu) equipped with an integrating sphere in the wavelength range of 300–800 nm, with $BaSO_4$ serving as the non-absorbing reference material. X-ray photoelectron spectroscopic (XPS) measurements were performed to examine the surface composition and chemical state of elements on the photocatalyst's surface. High-resolution (HR) XPS spectra were recorded using a PHI 5000 VersaProbeTM - Scanning ESCA Microprobe (ULVAC-PHI, Chigasaki Japan) instrument with monochromatic Al Kα irradiation (hν = 1486.6 eV). The binding energy (BE) for the C 1 s peak at 284.8 eV was used as the reference for calibration. FTIR spectroscopy was utilized to record the spectra of the photocatalysts in the range of 400–3200 cm^{-1} in diffuse reflectance mode. A Nicolet iS10 FTIR spectrometer with a resolution of 8 cm^{-1} was used at room temperature. The samples were prepared by diluting 10 % of the photocatalyst in KBr.

2.1. TEM imaging

For the needs of TEM, the powder was mechanically transferred to an amorphous carbon film on a copper mesh substrate (Agar S160, Agar Scientific), and excess was gently blown away with compressed air. After preparation, the samples were stored in a vacuum desiccator and then imaged with a transmission electron microscope (Hitachi H-800, Hitachi HighTechnologies). After selecting the imaging site, the sample was removed from the microscope and repeatedly placed in the climatic chamber (KK, Pol-Eko) at a temperature of 20 °C, pressure between 1000 and 1025 hPa and relative humidity in the range of 90 % to 95 %. They returned to the same observation site to observe structural changes with increasing exposure to water vapor. Due to the irreversible degradation of the material, each sample was tested once.

2.2. Preparation of $Cs_3Bi_2Br_9$

$Cs_3Bi_2Br_9$ was synthesized using the *Ligand-Assisted Reprecipitation Procedure* (LARP) technique, as previously described in our previous work [11]. The typical experimental process is as follows:

A three-necked round-bottom flask connected to a Schlenk line apparatus was charged with solid precursors (1.6 mmol of CsBr and 1.072 mmol of $BiBr_3$) and a mixture of solvents, DMSO (12 mL) and OLAm (132 μL). The prepared precursor solution was preheated to 70 °C under a nitrogen atmosphere. Simultaneously, an antisolvent was prepared by mixing 50 mL of anhydrous ethanol with 5 mL of OA, also under an inert atmosphere. The antisolvent was then heated to boiling at 83 °C. Subsequently, 10 mL of the warm precursor solution was slowly added dropwise into the boiling antisolvent while maintaining reflux. After the complete dropwise addition of the solution, the reaction was allowed to continue for 1 minute and immediately quenched by immersing the flask in an ice bath. After cooling to room temperature, the resulting $Cs_3Bi_2Br_9$ perovskite powder was washed sequentially with ethanol six times, with centrifugation at 6000 rpm performed after each wash step. Finally, the pure product was dried at 60 °C until all remaining ethanolic residues completely evaporated. Before use in the synthesis of $Cs_3Bi_2Br_9$ powder, both OLAm, and OA were dried at 100 °C for 2 h in the Schlenk line.

2.3. Encapsulation $Cs_3Bi_2Br_9$ in polythiophene

The chemical oxidative polymerization method was employed to prepare Pth/$Cs_3Bi_2Br_9$ samples with varying thicknesses of the polymeric layer on the perovskite surface [36]. First, 0.5 g of $Cs_3Bi_2Br_9$ perovskite was placed into a beaker, and 10 mL of chloroform was added. The resulting suspension was vigorously stirred for 0.5 h. Then, the appropriate amount of thiophene (TP) monomer was added to the suspension, with molar ratios of TP to perovskite set at 2:1, 9:1, and 22.6:1. The mixture was stirred for an additional 0.5 h to allow TP monomers to absorb onto the perovskite surface. Meanwhile, a separate solution of anhydrous $FeCl_3$ in chloroform was prepared. This solution was then added to the suspension mentioned above in order to initiate the polymerization process. The molar ratio of $FeCl_3$ to TP was 3:1. The polymerization reaction was allowed to proceed under a natural ambient atmosphere for 24 h. In the next step, methanol was added to the reaction mixture, causing a change in the chemical state of the polymer from an oxidizing to a reducing state. This change was visually apparent as the color of the powder shifted from black to reddish. Finally, the Pth/$Cs_3Bi_2Br_9$ products were washed with methanol five times, with centrifugation at 6000 rpm performed after each wash. The

samples were then dried at 60 °C overnight. Using the as-described procedure, samples with different amounts of Pth on $Cs_3Bi_2Br_9$ were obtained and designated as (2:1)Pth/$Cs_3Bi_2Br_9$, (9:1)Pth/$Cs_3Bi_2Br_9$, and (22.6:1)Pth/$Cs_3Bi_2Br_9$.

2.4. Photocatalytic performance

The photocatalytic activity of all the obtained samples was evaluated using the toluene degradation process. Toluene, a volatile organic compound (VOC), was chosen as a model air pollutant. The photocatalytic measurements were conducted in a stainless steel reactor with a total volume of 30 mL, equipped with a quartz window, two valves, and a rubber septum. Irradiation was provided by an array of UV (λ_{max} = 365 nm) and Vis (λ_{max} = 415 nm) LEDs, with intensities of 34.3 and 1.3 mW/cm^2, respectively. In a typical procedure, 20 mg of photocatalyst was dispersed in 2 mL of anhydrous ethanol using an ultrasonic bath for 10 min at 35 kHz. The resulting suspension was then slowly dropped onto a Petri dish (⌀ = 2.8 cm, h = 0.5 cm), and the sample was dried at 60 °C until complete evaporation of the liquid. This method ensured a well-spread layer of the sample for photocatalytic measurements. Each of the as-prepared samples was positioned at the bottom of the photoreactor, and the reactor was sealed with a quartz window. The gaseous toluene (C_0 = 50 ppm) was introduced into the reactor by opening the valves for 1 minute at a flow rate of 15 L/min. After this initial period, the valves were closed, and the system was kept without light for 15 min to establish an adsorption–desorption equilibrium between the toluene molecules and the photocatalyst particles. Next, a gaseous reference sample was collected through the septum using a syringe, and the irradiation was immediately initiated. Similarly, additional control samples were collected after 20, 40, and 60 min of irradiation using the same procedure. The concentration of toluene in the collected samples was determined using a gas chromatograph (GC-2010 Gas Chromatograph Plus Shimadzu) equipped with a 30 m × 0.25 mm Elite-5 MS capillary column (0.25 μm film thickness) and a flame ionization detector (FID). The samples (200 μL) were injected using a gas-tight syringe, and oxygen, air, and hydrogen were utilized as carrier gases at a flow rate of 3 mL/min. A gas chromatograph with a QP2010SE mass spectrometer (Shimadzu, Maryland, USA) was used to identify toluene degradation products. The gas chromatograph was equipped with an Rtx-5 capillary column with an inner diameter of 30 m × 0.25 mm (Restek) with a layer thickness of 0.25 μm. Analyses were carried out under programmed temperature conditions: from 40 °C for 4 min, then a rise of 10 °C min^{-1} to 220 °C, and finally 2 min at the final temperature. The injector temperature was 210 °C, and the gas sample was introduced in splitless mode for 1 min. The gas flow in the column was carried out at a constant pressure of 100 kPa. The temperature of the transfer line was 200 °C. The mass spectrometer was operated in SIM (Single Ion Monitoring; 8.5–9 min *m/z* 77, 105, 106 and 10.0–10.7 min *m/z* 79, 107, 108) or TIC (Total Ion Current) mode. Three scans per second were recorded. To determine the increase in CO_2 concentration after 1 h of the photocatalytic process, a gaseous sample (200 μL) was collected and subjected to analysis using gas chromatography with a thermal conductivity detector (GC/TCD, TRACE 1300; Thermo-Scientific), equipped with a HayeSep Q (100/120) column (Restek). Nitrogen was employed as the carrier gas at a flow rate of 1 mL/min.

To enhance our comprehension of the photocatalytic mechanism, we conducted measurements of the photocatalytic activities while introducing scavengers targeting specific chemical species potentially involved in the degradation of toluene molecules. To diminish the reactivity of the generated $O_2^{\bullet-}$, e^-, h^+, and $OH^\bullet$, we employed *p*–Benzoquinone (BQ), $AgNO_3$, ammonium oxalate (OA), and tert–butanol (Bu) as scavengers, respectively. Additionally, butylated hydroxytoluene (BHT) served as a scavenger for carbon sp3 radicals. Each scavenger (3 mg) was added to the suspension (20 mg of photocatalyst, 2 mL of ethanol), from which plates (Petri dishes) were prepared for photocatalytic tests.

To assess the stability of the photocatalysts during photocatalytic experiments, two different samples, namely bare $Cs_3Bi_2Br_9$ and (9:1) Pth/$Cs_3Bi_2Br_9$, were subjected to four sequential photocatalytic cycles. At the end of each cycle, the system was opened, and the photocatalyst surface was regenerated by exposing it to UV light (UV LEDs) for an additional 30 min. This regeneration step aimed to remove any adsorbed intermediate products from the toluene decomposition process.

3. Results

3.1. XRD

Fig. 1 presents the powder X-ray diffraction (PXRD) patterns of both the pristine $Cs_3Bi_2Br_9$ and $Cs_3Bi_2Br_9$ samples modified with three different thicknesses of Pth layers. Within Fig. 1, the red solid line represents a profile fit using the LeBail method, and the green vertical marks indicate the expected Bragg reflections. The refined lattice parameters are listed in Table 1. Furthermore, the summary of the crystallographic planes evaluated in the photocatalysts tested is shown in Table S1. It is evident that both the pristine $Cs_3Bi_2Br_9$ and the $Cs_3Bi_2Br_9$ samples modified with Pth layers share the same trigonal crystal structure (P-3 m1). In the case of lattice parameters for the pristine $Cs_3Bi_2Br_9$ and the $Cs_3Bi_2Br_9$ sample with the thickest Pth layer on its surface ((2:1) Pth / $Cs_3Bi_2Br_9$), they exhibit similar values and are in agreement with those reported in the literature [37]. However, for samples with thicker Pth layers on $Cs_3Bi_2Br_9$, a decrease in these values was observed. This phenomenon indicates that during the in situ polymerization of Pth on

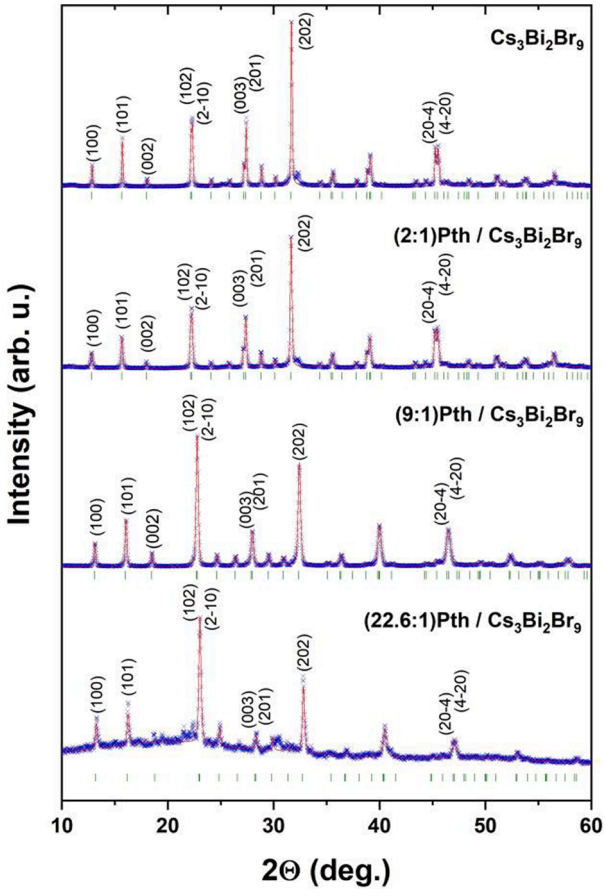

Fig. 1. Powder x-ray diffraction patterns for pristine and Pth-modified $Cs_3Bi_2Br_9$ samples. Experimental data are depicted with blue "x" symbols, while the calculated profile and expected Bragg reflections are represented by a red line and green vertical ticks. (For interpretation of the references to color in this figure legend, the reader is referred to the web version of this article.)

Table 1
Refined lattice parameters for pristine $Cs_3Bi_2Br_9$ and Pth-modified $Cs_3Bi_2Br_9$.

Sample label	a	c	Crystal structure
$Cs_3Bi_2Br_9$	7.9683(3)	9.8431(4)	Trig. s.g. P-3m1 (#164)
(2:1)Pth/$Cs_3Bi_2Br_9$	7.9685(4)	9.8454(5)	Trig. s.g. P-3m1 (#164)
(9:1)Pth/$Cs_3Bi_2Br_9$	7.8012(5)	9.5975(8)	Trig. s.g. P-3m1 (#164)
(22.6:1)Pth/$Cs_3Bi_2Br_9$	7.736(3)	9.444(4)	Trig. s.g. P-3m1 (#164)

the perovskite surface, the $FeCl_3$ oxidizing agent used had an influence on the $Cs_3Bi_2Br_9$ structure, leading to a slight doping effect with Cl ions, which are smaller than Br ions [11].

Furthermore, pristine $Cs_3Bi_2Br_9$ and the sample (9:1)Pth / $Cs_3Bi_2Br_9$, which showed the highest photoactivity in the field of UV-LED irradiation, were re-examined in the XRD analysis after 1st and 4th cycle of photocatalytic stability test. The obtained XRD patterns are shown in Figure S1 and the lattice parameters are listed in Table S2. Compared to the pristine $Cs_3Bi_2Br_9$ and the composite (9:1)Pth / $Cs_3Bi_2Br_9$ before photocatalytic processes, no differences were observed in the diffractograms.

3.2. Optical properties

To analyze the light absorption properties of the synthesized materials, UV–Vis/DRS spectra were recorded in the wavelength range of 300–800 nm and are presented in Fig. 2. The unmodified $Cs_3Bi_2Br_9$ perovskite exhibited absorption bands in both the UV and visible (Vis) regions, extending up to approximately 480 nm. Additionally, a characteristic peak corresponding to the n = 1 excitonic transition at around 421 nm was observed. This observation is consistent with the behavior typically observed in Bi-based halide perovskite structures [11,38,39], and the determined value aligns with the literature reports for the Br–analog [11]. Furthermore, for $Cs_3Bi_2Br_9$ coated with the thinnest Pth layer ((2:1)Pth/$Cs_3Bi_2Br_9$), a blue shift in the absorption band towards shorter wavelengths was achieved. As a result, the excitonic transition peak was also shifted to approximately 390 nm. Moreover, a significant enhancement in the absorption intensity within the visible light range was observed for samples with thicker Pth layers on the perovskite surface ((9:1)Pth/$Cs_3Bi_2Br_9$ and (22.6:1)Pth/$Cs_3Bi_2Br_9$) due to the dominant presence of the polymer in these samples. This effect led to the extinction of the excitonic transition peak, making it not visible in the spectra shown in Fig. 2.

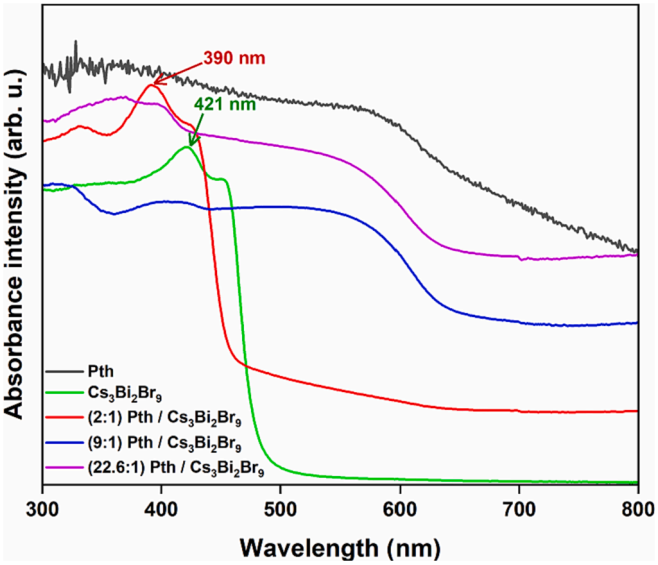

Fig. 2. UV–Vis/DRS spectra of Pth, bare $Cs_3Bi_2Br_9$, and Pth-modified $Cs_3Bi_2Br_9$.

3.3. FT-IR

The Fourier-transform infrared (FT–IR) spectra of the prepared samples, including the Pth, the nonmodified $Cs_3Bi_2Br_9$ and the Pth–modified $Cs_3Bi_2Br_9$ samples, were recorded and are presented in Fig. 3. In all polymer-modified samples and pure Pth, C–H stretching vibrations were observed in the range of 2800–3000 cm^{-1} [36,40]. However, only the samples with thicker Pth layers ((9:1)Pth/$Cs_3Bi_2Br_9$ and (22.6:1)Pth/$Cs_3Bi_2Br_9$) exhibited additional characteristic bands corresponding to the presence of polythiophene. Of particular importance is the peak observed at 787 cm^{-1}, which can be attributed to the out-of-plane C–H vibration of the 2,5–substituted thiophene ring. This finding suggests that during the polymerization reaction, there is a preference for bonding at the 2– and 5– positions of the thiophene monomer. Furthermore, the spectrum of the (22.6:1)Pth/$Cs_3Bi_2Br_9$ composite also displays symmetric C = C stretching vibrations at 1435 cm^{-1} [40,41]. Additionally, a signal at 1032 cm^{-1} and two signals at 1118 cm^{-1} and 1218 cm^{-1} were identified, corresponding to the Cβ–H bending vibration and Cα–Cα stretching vibrations, respectively, providing evidence of Cα–Cα connections [36,42]. Overall, the presence of these characteristic bands confirms the successful polymerization reactions in the Pth–modified samples. Moreover, FTIR spectra were also recorded for pristine $Cs_3Bi_2Br_9$ and the (9:1)Pth / $Cs_3Bi_2Br_9$ composite after the first photocatalytic process and after the fourth one. The results and description are presented in the Supporting materials.

3.4. XPS

The surface elemental composition of bare $Cs_3Bi_2Br_9$ and Pth/$Cs_3Bi_2Br_9$ composites evaluated by XPS is presented in Table 2. The

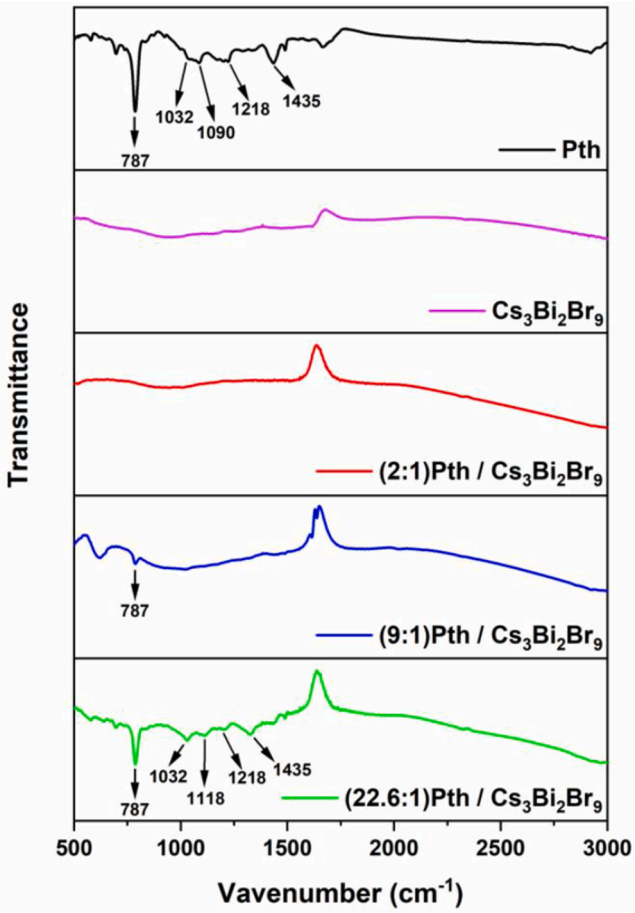

Fig. 3. FT-IR spectra of Pth, bare $Cs_3Bi_2Br_9$ and Pth-modified $Cs_3Bi_2Br_9$.

Table 2
Elemental contents in the surface layer of bare $Cs_3Bi_2Br_9$ and polythiophene (Pth) / $Cs_3Bi_2Br_9$ composites, evaluated by XPS.

	Elemental composition (atomic %.)							
Sample label	Cs	Bi	Br	C	O	S	C/(Cs + Bi + Br)	S/(Cs + Bi + Br)
$Cs_3Bi_2Br_9$	7.36	21.36	35.82	21.70	13.76	0	0.34	0
(2:1)Pth/$Cs_3Bi_2Br_9$	7.93	6.79	18.99	51.84	10.62	3.83	1.54	0.11
(9:1)Pth/$Cs_3Bi_2Br_9$	0.31	9.73	5.50	64.33	8.13	12.00	4.14	0.77
(22.6:1)Pth/$Cs_3Bi_2Br_9$	1.12	0.83	3.14	75.99	2.18	16.74	14.93	3.29

chemical character of elements, detected in both pristine $Cs_3Bi_2Br_9$ and one of the Pth-modified $Cs_3Bi_2Br_9$ composite are identified and described in the deconvoluted HR spectra displayed in Fig. 4. The HR spectra of Cs3d, Bi4f, and Br3d agree well with spectral features reported for similar composites [11,43]. Please note that the intensity of Cs3d, Bi4f, and Br3d spectra recorded for the (9:1)Pth/$Cs_3Bi_2Br_9$ is much lower than the corresponding one of pristine $Cs_3Bi_2Br_9$. That indicates the effective encapsulation of $Cs_3Bi_2Br_9$ in Pth. The Bi4f spectrum of the Pth-modified $Cs_3Bi_2Br_9$ is overlapped by S2p signals. Deconvolution of this complex spectrum allows separating the S2p spectrum features and identifying well sulfur in Pth (S 2p3/2 at BE close to 164.3 eV) [44,45]. The presence of sulfur is also confirmed by the C 1 s spectrum (C-S bound identified at BE of 285.5 eV [46]). In contrast, the Br 3d spectrum shows two chemical states of bromine. The first is characteristic of $Cs_3Bi_2Br_9$ (Br $3d_{5/2}$ signal near 69.0 eV), and the second, represented by the Br $3d_{5/2}$ signal located at 70.5 eV, can be attributed to the binding of bromine to the Pth carbon. A similar BE (70.0 ± 0.2 eV) XPS value was recently reported for Cx-Br surface complexes [46]. The increase of Pth content on the (2:1)Pth/$Cs_3Bi_2Br_9$, (9:1)Pth/$Cs_3Bi_2Br_9$, and (22.6:1)Pth/$Cs_3Bi_2Br_9$ samples is confirmed by the increasing values of C/(Cs + Bi + Br) and S/(Cs + Bi + Br) ratios in Table 2.

3.5. TEM imaging

To see the morphological changes of the material in the function of exposure to water, the ex-situ approach was utilized and the diffraction patterns were analyzed. The chosen particle was first observed before the exposure to water vapor and its diffraction pattern is consistent with the $Cs_3Bi_2Br_6$ reference (Fig. 5), however, the diffraction spots forming the inner ring indicate the presence of (001) lattice planes of oxidized phase, which is a result of initial degradation of the material stored in air. After 1 s of interaction with the water, the particle changed its morphology drastically. The diffraction analysis showed the partial oxidation of perovskite as the unfamiliar spots corresponding to BiOBr appeared in the pattern (Fig. 5). The process was more visible after 5, 10 and 15 s of interaction with water in both particle's morphology and diffraction pattern, which at the end was almost fully correlated with BiOBr phase. The material was degrading more with every exposure, resulting in the expanded, frayed structure.

In the case of encapsulated perovskite, the results were different

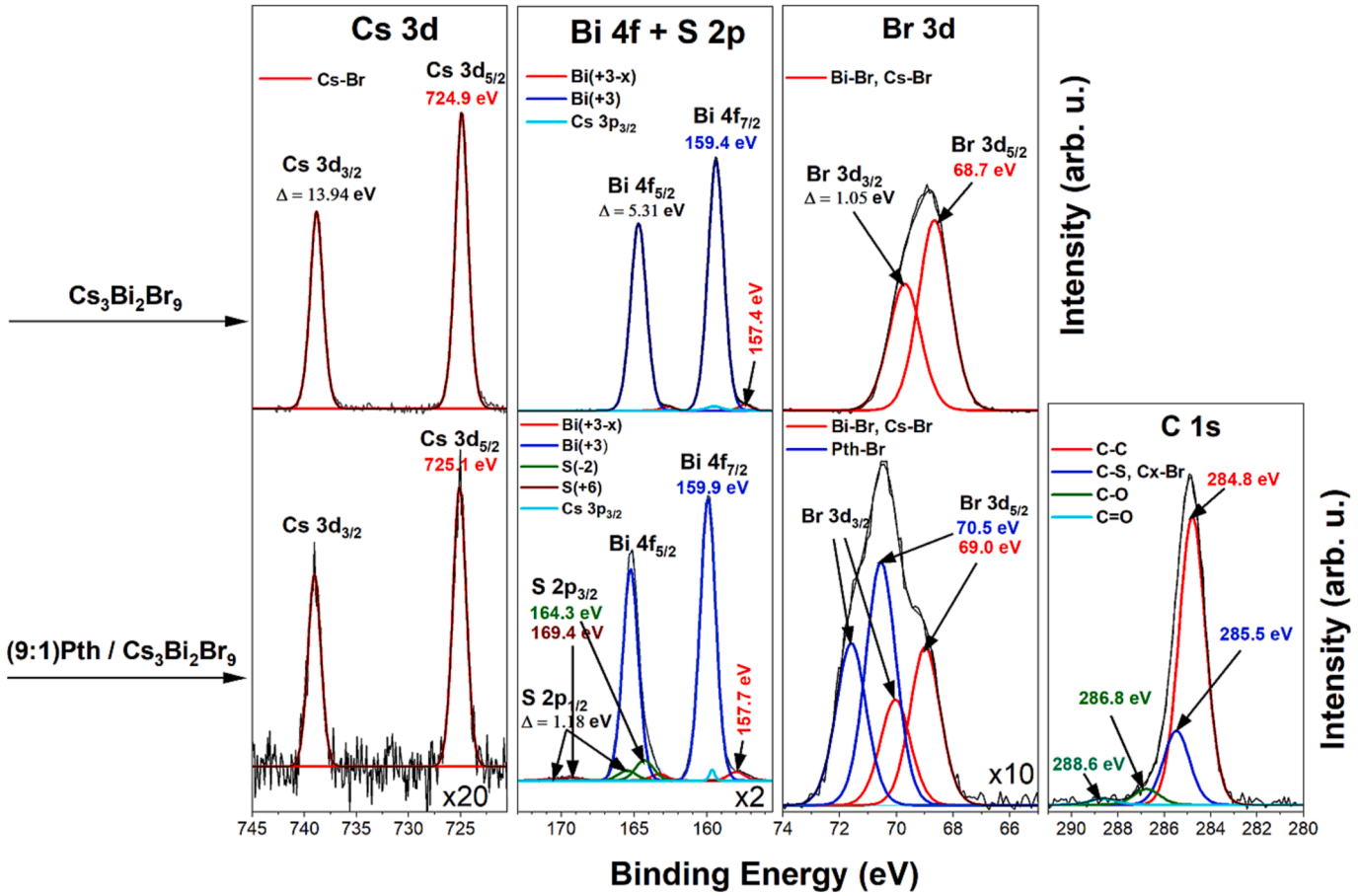

Fig. 4. High resolution Cs 3d, Bi 4f, S 2p, Br 3d and C 1s XPS spectra recorded for bare $Cs_3Bi_2Br_9$ and (9:1)Pth/$Cs_3Bi_2Br_9$ composite. The BE of the main signals are noted and the spin orbit separation (Δ) is given as well.

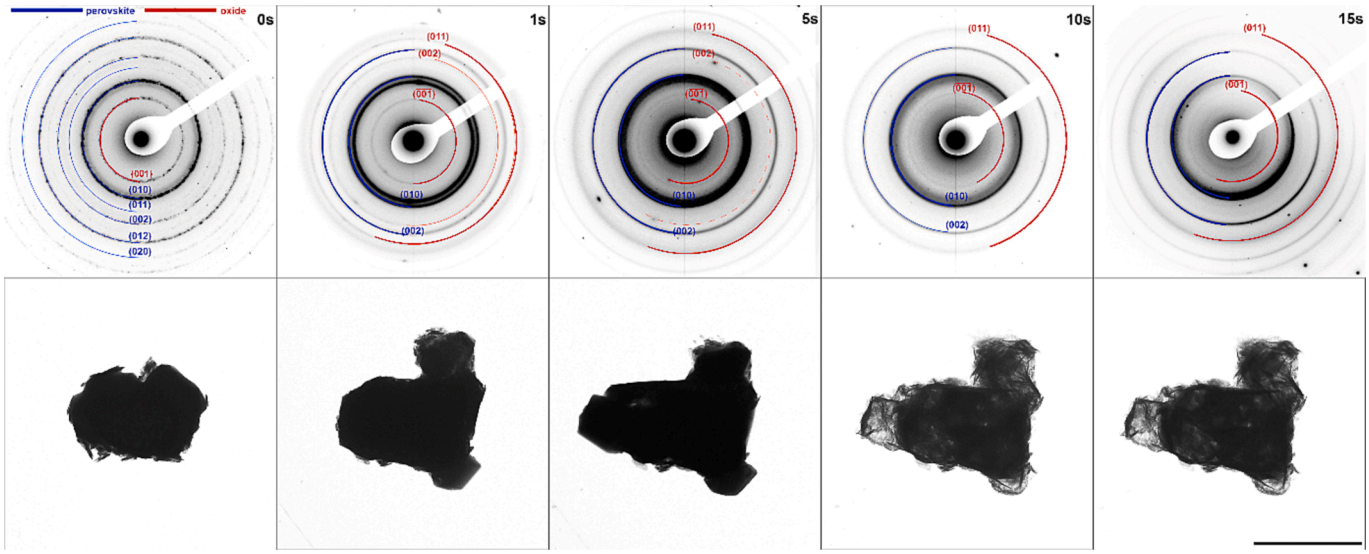

Fig. 5. Diffractional (a-e) and microstructural (f-j) degradation of $Cs_3Bi_2Br_9$. The reaction from $Cs_3Bi_2Br_9$ to BiOBr is largely carried out in the first contact with the water vapor, but the change in morphology continues until the 15 s exposure. The scale bar presents 1 μm.

depending on the polymer content. The sample (2:1)Pth/$Cs_3Bi_2Br_9$ degraded partly after 5 s of exposure to water (Fig. 6 b), however, the morphological changes were much less visible than in the case of uncoated material (Fig. 5). The particle could be easily recognized with increasing exposure time up to 15 s as the oxidation effects were slight (Fig. 6 c). In both cases, the diffraction patterns did not show the presence of the BiOBr phase (Fig. 6 e,f). The encapsulation of (9:1)Pth/$Cs_3Bi_2Br_9$ seems to be the most efficient way to prevent material oxidation, as its morphology did not change at all, even after long exposure to water (Fig. 6 g-i). The corresponding diffraction patterns (Fig. 6 j-l) did now show any spots coming from the BiOBr phase, but only from $Cs_3Bi_2Br_9$. In all cases, diffractions were collected over a much wider area than just one microparticle. The general, lower visibility of the diffraction points in encapsulated samples is due to the tendency of the sample to aggregate into electron-non-transparent areas.

3.6. Photoactivity

Photocatalytic activity of the obtained materials was evaluated in the degradation reaction of toluene, as a model air pollutant, under UV-LEDs (λ_{max} = 365 nm) and Vis-LEDs (λ_{max} = 415 nm) irradiation. None of the photocatalysts exhibited activity upon excitation in the field of Vis light, unlike under UV light. The synthesized materials show high absorption of light in the visible range, hence from a theoretical point of view, the proposed photocatalysts should also show activity under Vis light, but the lack of activity is probably caused by too low intensity of Vis irradiation (1.3 mW/cm^2) compared to the intensity of irradiation emitted by UV diodes (34.3 mW/cm^2). All photoactivity results are shown in Fig. 7. Among the samples, the (9:1)Pth/$Cs_3Bi_2Br_9$ composite showed the highest photoactivity, with an efficiency of toluene degradation reaching approximately 45.6 % after 1 h of irradiation. In comparison, the nonmodified $Cs_3Bi_2Br_9$ perovskite exhibited a toluene degradation efficiency of less than 40 %. In both cases, toluene absorption reached around 25 % after 1 h without irradiation. For the sample with the highest photoactivity, (9:1)Pth / $Cs_3Bi_2Br_9$, tests were conducted in the presence of appropriate scavengers. A decrease in the efficiency of toluene degradation was observed when $AgNO_3$ and BQ were introduced (Fig. 7b). This indicates that photogenerated electrons and $O_2^{\bullet-}$ are responsible for toluene degradation, respectively. Additionally, a reaction was carried out using BHT, which inhibits the reaction of radicals generated on sp3 carbon. In this case, a decrease in the efficiency of toluene degradation was observed, providing evidence that the reaction occurs at the methyl group in the toluene molecule. According to the literature, the intermediate products of the reaction are benzaldehyde and, to a lesser extent, benzyl alcohol [47,48]. In our study, we detected benzaldehyde after one hour of exposure and recorded an increase in CO_2 concentration. Hence, we conclude that the contamination was partially mineralized. The recorded chromatograms are presented in the Supplementary Information (Figures S3-S6).

Furthermore, a photocatalytic stability test was conducted for four sequential photocatalytic cycles for both pristine $Cs_3Bi_2Br_9$ perovskite and the (9:1)Pth/$Cs_3Bi_2Br_9$ composite. The results are presented in Fig. 7c and 7d. It was clearly observed that the degradation efficiency decreased more significantly in the cycles involving bare $Cs_3Bi_2Br_9$. The toluene degradation efficiency decreased from 39.8 % in the first cycle to 28.9 % in the fourth cycle for bare $Cs_3Bi_2Br_9$, while for the (9:1)Pth/$Cs_3Bi_2Br_9$ composite, the efficiency decreased from 46.5 % to 46 % over the same cycles. This phenomenon demonstrates the increased stability of the polymer–wrapped perovskite during the activity tests.

The proposed mechanism for the photocatalytic oxidation of toluene in the presence of (9:1)Pth/$Cs_3Bi_2Br_9$ as the photocatalyst under UV-LEDs irradiation is illustrated in Fig. 8. Upon irradiation with UV light, both the polymer (Pth) and perovskite ($Cs_3Bi_2Br_9$) components undergo electron excitation, leading to the generation of electron-hole pairs. The electrons from the lowest unoccupied molecular orbital (LUMO) level of the polymer possess a higher potential than the conduction band (CB) of the perovskite, allowing for electron transfer to the perovskite. Furthermore, the photoexcited electrons in the LUMO of the polymer and the CB of the perovskite exhibit a potential higher than −0.33 V ($O_2/O_2^{\bullet-}$), enabling the formation of superoxide radicals ($O_2^{\bullet-}$) as the primary species responsible for the oxidation of toluene particles adsorbed on the surface of the photocatalyst (see Fig. 8).

4. Conclusion

In this study, we focused on investigating the photoactivity and stability of $Cs_3Bi_2Br_9$, a lead-free bismuth-based halide perovskite, in a humid environment. Consistent with our previous experiments, we observed the complete instability of the perovskite when exposed to water molecules [11]. To examine this phenomenon, we utilized transmission electron microscopy (TEM) imaging to track the changes in the microstructure of the perovskite over time. The results revealed immediate decomposition of the perovskite upon contact with water vapor. To overcome this instability, we successfully encapsulated the

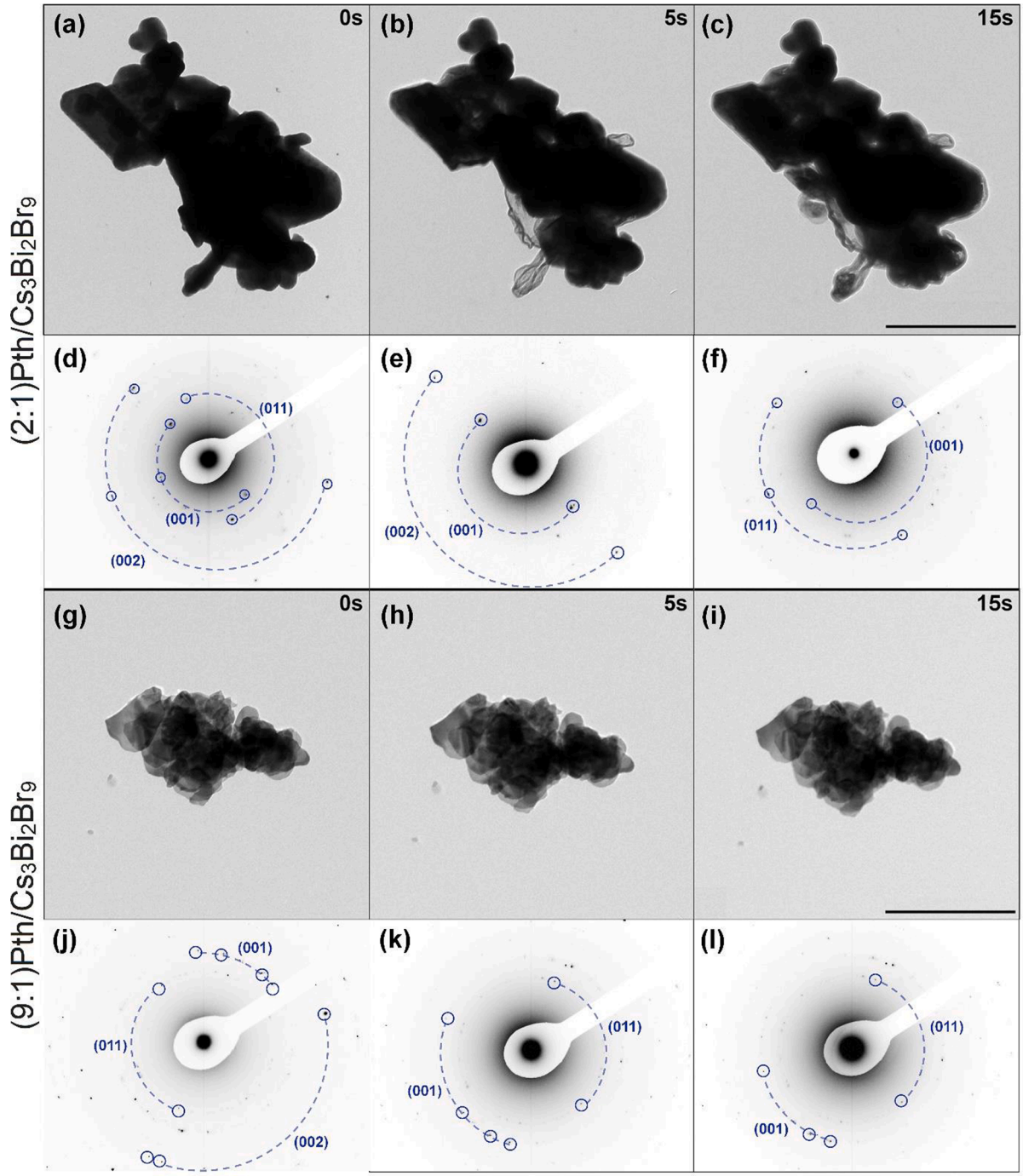

Fig. 6. Microstructural and diffractional degradation (2:1)Pth/$Cs_3Bi_2Br_9$ (a-e) and (9:1)Pth/$Cs_3Bi_2Br_9$ (f-j) of polythiophene. (2:1)Pth/$Cs_3Bi_2Br_9$ still shows morphological degradation after 5 s exposure, while the (9:1)Pth/$Cs_3Bi_2Br_9$ can slow down the degradation processes, visible both on microstructure and electron diffraction. Diffraction patterns do not show BiOBr peaks. The scale bar presents 1 μm.

perovskite within a polymer matrix. By controlling the monomer concentration during an in situ polymerization reaction on the perovskite surface, we achieved three different polymer thicknesses on $Cs_3Bi_2Br_9$ particles. Subsequently, stability tests were conducted using TEM imaging and photocatalytic performance was evaluated of each sample. The results clearly demonstrated the enhanced stability of the composite material where the perovskite was embedded in the polythiophene matrix. Additionally, photocatalytic experiments revealed a synergistic effect between the conductive polymer and the perovskite in the toluene decomposition reaction. Among the samples tested, (9:1)Pth/$Cs_3Bi_2Br_9$ exhibited the highest photoactivity. We performed four cycles of photoactivity tests for both the (9:1)Pth/$Cs_3Bi_2Br_9$ composite and the bare perovskite to compare their performance. The results further supported the increased photostability of the sample containing the polymer. Based on these findings, we proposed a possible mechanism for the photocatalytic reactions observed, which is unprecedented in the literature for the synthesized Pth/$Cs_3Bi_2Br_9$ system.

CRediT authorship contribution statement

Magdalena Miodyńska: Investigation, Methodology, Data curation, Writing – original draft, Visualization, Conceptualization, Project

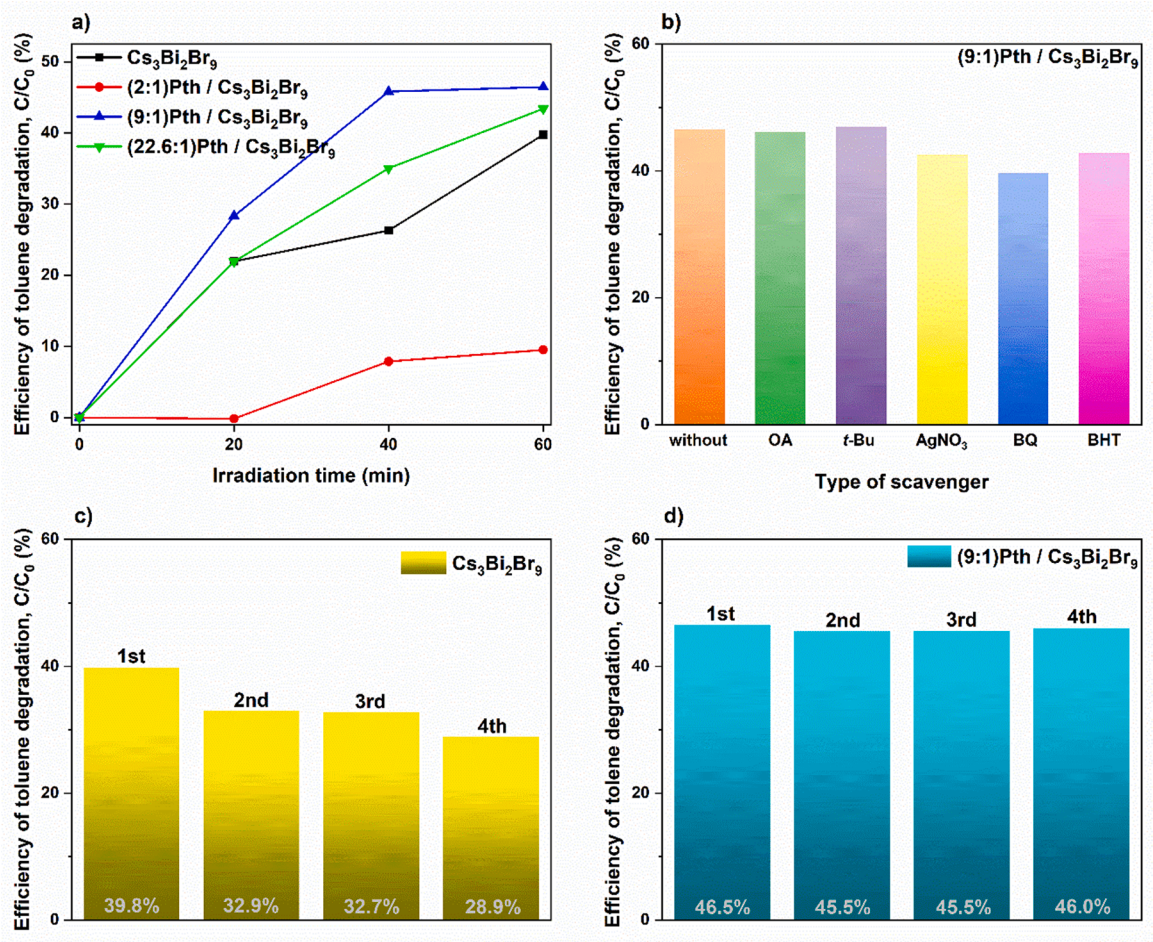

Fig. 7. Photocatalytic activity of a) bare $Cs_3Bi_2Br_9$ and $Cs_3Bi_2Br_9$ modified with different amounts of Pth under UV light (UV LEDs λ_{max} = 365 nm), b) efficiency of toluene degradation over (9:1)Pth / $Cs_3Bi_2Br_9$ sample with and without the presence of scavengers and c, d) bare $Cs_3Bi_2Br_9$ and (9:1)Pth/$Cs_3Bi_2Br_9$ in four sequential photocatalytic cycles also under UV light (UV LEDs λ_{max} = 365 nm).

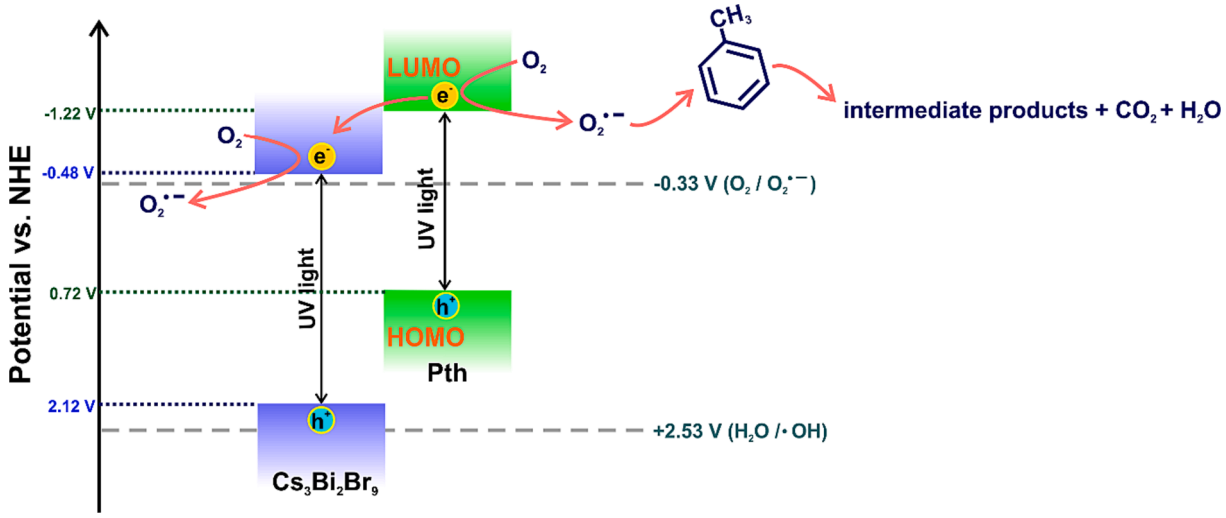

Fig. 8. Schematic illustration of the photocatalytic performance to toluene degradation over Pth/$Cs_3Bi_2Br_9$ photocatalyst under UV light (λ_{max} = 365 nm) [11,49].

administration, Funding acquisition. **Olga Kaczmarczyk:** Investigation, Methodology, Data curation, Writing – original draft, Visualization, Conceptualization. **Wojciech Lisowski:** Investigation, Writing – original draft, Visualization. **Andrzej Żak:** Investigation, Methodology, Data curation, Writing – original draft, Visualization, Conceptualization. **Tomasz Klimczuk:** Investigation, Methodology, Visualization. **Monika Paszkiewicz:** Investigation, Methodology, Visualization, Writing – original draft. **Adriana Zaleska-Medynska:** Supervision, Resources.

Declaration of Competing Interest

The authors declare that they have no known competing financial interests or personal relationships that could have appeared to influence the work reported in this paper.

Data availability

Data will be made available on request.

Acknowledgments

This research was financially supported by the National Science Center of Poland (grant 2018/29/N/ST5/00496: "Metal halide perovskites for heterogeneous photocatalysis"). O.K. and A.Z. would like to thank F.M. Ross and K. Reidy (Massachusetts Institute of Technology, Cambridge, USA) for access to equipment and environmental TEM imaging trials.

Appendix A. Supplementary material

Supplementary data to this article can be found online at https://doi.org/10.1016/j.apsusc.2023.158725.

References

[1] J. Cao, F. Yan, Recent progress in tin-based perovskite solar cells, Energy Environ. Sci. 14 (2021) 1286–1325, https://doi.org/10.1039/D0EE04007J.
[2] M.M. Byranvand, W. Zuo, R. Imani, M. Pazoki, M. Saliba, Tin-based halide perovskite materials: properties and applications, Chem. Sci. 13 (2022) 6766–6781, https://doi.org/10.1039/D2SC01914K.
[3] F.J. Iftikhar, Q. Wali, S. Yang, Y. Iqbal, R. Jose, S. Munir, I.A. Gondal, M.E. Khan, Structural and optoelectronic properties of hybrid halide perovskites for solar cells, Org. Electron. 91 (2021), 106077, https://doi.org/10.1016/j.orgel.2021.106077.
[4] M. Pitaro, E.K. Tekelenburg, S. Shao, M.A. Loi, Tin halide perovskites: from fundamental properties to solar cells, Adv. Mater. 34 (2022) 2105844, https://doi.org/10.1002/adma.202105844.
[5] W.-J. Yin, T. Shi, Y. Yan, Unique properties of halide perovskites as possible origins of the superior solar cell performance, Adv. Mater. 26 (2014) 4653–4658, https://doi.org/10.1002/adma.201306281.
[6] A.K. Jena, A. Kulkarni, T. Miyasaka, Halide perovskite photovoltaics: background, status, and future prospects, Chem. Rev. 119 (2019) 3036–3103, https://doi.org/10.1021/acs.chemrev.8b00539.
[7] Y. Dong, Y. Zou, J. Song, X. Song, H. Zeng, Recent progress of metal halide perovskite photodetectors, J. Mater. Chem. C. 5 (2017) 11369–11394, https://doi.org/10.1039/C7TC03612D.
[8] H. Lian, Y. Li, S. Saravanakumar, H. Jiang, Z. Li, J. Wang, L. Xu, W. Zhao, G. Han, Metal halide perovskite quantum dots for amphiprotic bio-imaging, Coord. Chem. Rev. 452 (2022), 214313, https://doi.org/10.1016/j.ccr.2021.214313.
[9] A.Y. Zhizhchenko, A.B. Cherepakhin, M.A. Masharin, A.P. Pushkarev, S. A. Kulinich, A.A. Kuchmizhak, S.V. Makarov, Directional lasing from nanopatterned halide perovskite nanowire, Nano Lett. 21 (2021) 10019–10025, https://doi.org/10.1021/acs.nanolett.1c03656.
[10] K. Ji, M. Anaya, A. Abfalterer, S.D. Stranks, Halide perovskite light-emitting diode technologies, Adv. Opt. Mater. 9 (2021) 2002128, https://doi.org/10.1002/adom.202002128.
[11] M. Miodyńska, A. Mikolajczyk, P. Mazierski, T. Klimczuk, W. Lisowski, G. Trykowski, A. Zaleska-Medynska, Lead-free bismuth-based perovskites coupled with g–C3N4: A machine learning based novel approach for visible light induced degradation of pollutants, Appl. Surf. Sci. 588 (2022), 152921, https://doi.org/10.1016/j.apsusc.2022.152921.
[12] H. Huang, B. Pradhan, J. Hofkens, M.B.J. Roeffaers, J.A. Steele, Solar-driven metal halide perovskite photocatalysis: design, stability, and performance, ACS Energy Lett. 5 (2020) 1107–1123, https://doi.org/10.1021/acsenergylett.0c00058.
[13] Y. Huang, T. Liu, D. Li, D. Zhao, A. Amini, C. Cheng, G. Xing, Limitations and solutions for achieving high-performance perovskite tandem photovoltaics, Nano Energy. 88 (2021), 106219, https://doi.org/10.1016/j.nanoen.2021.106219.
[14] Y. Yuan, G. Yan, R. Hong, Z. Liang, T. Kirchartz, Quantifying efficiency limitations in all-inorganic halide perovskite solar cells, Adv. Mater. 34 (2022) 2108132, https://doi.org/10.1002/adma.202108132.
[15] Y. Cui, L. Yang, X. Wu, J. Deng, X. Zhang, J. Zhang, Recent progress of lead-free bismuth-based perovskite materials for solar cell applications, J. Mater. Chem. C. (2022), https://doi.org/10.1039/D2TC02643K.
[16] A.H. Slavney, T. Hu, A.M. Lindenberg, H.I. Karunadasa, A bismuth-halide double perovskite with long carrier recombination lifetime for photovoltaic applications, J. Am. Chem. Soc. 138 (2016) 2138–2141, https://doi.org/10.1021/jacs.5b13294.
[17] Y. Zhou, Y. Zhao, Chemical stability and instability of inorganic halide perovskites, Energy Environ. Sci. 12 (2019) 1495–1511, https://doi.org/10.1039/C8EE03559H.
[18] D. Saikia, A. Betal, J. Bera, S. Sahu, Progress and challenges of halide perovskite-based solar cell- a brief review, Mater. Sci. Semicond. Process. 150 (2022), 106953, https://doi.org/10.1016/j.mssp.2022.106953.
[19] S. Thampy, W. Xu, J.W.P. Hsu, Metal oxide-induced instability and its mitigation in halide perovskite solar cells, J. Phys. Chem. Lett. 12 (2021) 8495–8506, https://doi.org/10.1021/acs.jpclett.1c02371.
[20] Y. Duan, D.-Y. Wang, R.D. Costa, Recent progress on synthesis, characterization, and applications of metal halide Perovskites@metal oxide, Adv. Funct. Mater. 31 (2021) 2104634, https://doi.org/10.1002/adfm.202104634.
[21] Z.-J. Li, E. Hofman, J. Li, A.H. Davis, C.-H. Tung, L.-Z. Wu, W. Zheng, Photoelectrochemically active and environmentally stable CsPbBr 3/TiO2 core/shell nanocrystals, Adv. Funct. Mater. 28 (2018) 1704288, https://doi.org/10.1002/adfm.201704288.
[22] V.K. Ravi, S. Saikia, S. Yadav, V.V. Nawale, A. Nag, CsPbBr 3/ZnS core/shell type nanocrystals for enhancing luminescence lifetime and water stability, ACS Energy Lett. 5 (2020) 1794–1796, https://doi.org/10.1021/acsenergylett.0c00858.
[23] X. Zhang, M. Lu, Y. Zhang, H. Wu, X. Shen, W. Zhang, W. Zheng, V.L. Colvin, W. W. Yu, PbS Capped cspbi3 nanocrystals for efficient and stable light-emitting devices using p–i–n structures, ACS Cent. Sci. 4 (2018) 1352–1359, https://doi.org/10.1021/acscentsci.8b00386.
[24] Z.-C. Kong, J.-F. Liao, Y.-J. Dong, Y.-F. Xu, H.-Y. Chen, D.-B. Kuang, C.-Y. Su, Core@Shell CsPbBr 3@zeolitic imidazolate framework nanocomposite for efficient photocatalytic CO2 reduction, ACS Energy Lett. 3 (2018) 2656–2662, https://doi.org/10.1021/acsenergylett.8b01658.
[25] S.K. Yadav, G.K. Grandhi, D.P. Dubal, J.C. de Mello, M. Otyepka, R. Zbořil, R. A. Fischer, K. Jayaramulu, Metal halide perovskite@metal-organic framework hybrids: synthesis, design, properties, and applications, Small 16 (2020) 2004891, https://doi.org/10.1002/smll.202004891.
[26] H. Shankar, S. Ghosh, P. Kar, Boosting the stability of lead halide perovskite nanocrystals by metal–organic frameworks and their applications, J. Mater. Chem. C. 10 (2022) 11532–11554, https://doi.org/10.1039/D2TC02243E.
[27] S.N. Raja, Y. Bekenstein, M.A. Koc, S. Fischer, D. Zhang, L. Lin, R.O. Ritchie, P. Yang, A.P. Alivisatos, Encapsulation of perovskite nanocrystals into macroscale polymer matrices: enhanced stability and polarization, ACS Appl. Mater. Interfaces. 8 (2016) 35523–35533, https://doi.org/10.1021/acsami.6b09443.
[28] B. McKenna, J.R. Troughton, T.M. Watson, R.C. Evans, Enhancing the stability of organolead halide perovskite films through polymer encapsulation, RSC Adv. 7 (2017) 32942–32951, https://doi.org/10.1039/C7RA06002E.
[29] Y. Hu, J. Shu, X. Zhang, A. Zhao, Y. Liu, R. Li, Y. Di, H. Xu, Z. Gan, Encapsulation of colloid perovskite nanocrystals into solid polymer matrices: Impact on electronic transition and photoluminescence, J. Lumin. 219 (2020), 116938, https://doi.org/10.1016/j.jlumin.2019.116938.
[30] Z. Zhang, L. Liu, H. Huang, L. Li, Y. Wang, J. Xu, J. Xu, Encapsulation of CsPbBr 3 perovskite quantum dots into PPy conducting polymer: exceptional water stability and enhanced charge transport property, Appl. Surf. Sci. 526 (2020), 146735, https://doi.org/10.1016/j.apsusc.2020.146735.
[31] Y. Jiang, L. Qiu, E.J. Juarez-Perez, L.K. Ono, Z. Hu, Z. Liu, Z. Wu, L. Meng, Q. Wang, Y. Qi, Reduction of lead leakage from damaged lead halide perovskite solar modules using self-healing polymer-based encapsulation, Nat. Energy. 4 (2019) 585–593, https://doi.org/10.1038/s41560-019-0406-2.
[32] H. Liu, M. Siron, M. Gao, D. Lu, Y. Bekenstein, D. Zhang, L. Dou, A.P. Alivisatos, P. Yang, Lead halide perovskite nanowires stabilized by block copolymers for Langmuir-Blodgett assembly, Nano Res. 13 (2020) 1453–1458, https://doi.org/10.1007/s12274-020-2717-9.
[33] Y. Liu, T. Chen, Z. Jin, M. Li, D. Zhang, L. Duan, Z. Zhao, C. Wang, Tough, stable and self-healing luminescent perovskite-polymer matrix applicable to all harsh aquatic environments, Nat. Commun. 13 (2022) 1338, https://doi.org/10.1038/s41467-022-29084-z.
[34] Y. Zhang, B. Zhang, Y. Fu, Y. Han, T. Zhang, L. Zhang, J. Guo, X. Zhang, An ultrastable perovskite–polymer exciplex through self energy-level adaption for under-water light-emitting devices, J. Mater. Chem. C. 10 (2022) 8609–8616, https://doi.org/10.1039/D2TC01006B.
[35] T.-H. Han, J.-W. Lee, C. Choi, S. Tan, C. Lee, Y. Zhao, Z. Dai, N. De Marco, S.-J. Lee, S.-H. Bae, Y. Yuan, H.M. Lee, Y. Huang, Y. Yang, Perovskite-polymer composite cross-linker approach for highly-stable and efficient perovskite solar cells, Nat. Commun. 10 (2019) 520, https://doi.org/10.1038/s41467-019-08455-z.
[36] M. Khatamian, M. Fazayeli, B. Divband, Preparation, characterization and photocatalytic properties of polythiophene-sensitized zinc oxide hybrid nanocomposites, Mater. Sci. Semicond. Process. 26 (2014) 540–547, https://doi.org/10.1016/j.mssp.2014.04.038.
[37] M. St, Caesium Enneabromodibismuthate(lll) 9 (1975) 5–8.
[38] J. Gu, G. Yan, Y. Lian, Q. Mu, H. Jin, Z. Zhang, Z. Deng, Y. Peng, Bandgap engineering of a lead-free defect perovskite Cs3Bi2I9 through trivalent doping of Ru3+, RSC Adv. 8 (2018) 25802–25807, https://doi.org/10.1039/C8RA04422H.
[39] K.M. McCall, C.C. Stoumpos, O.Y. Kontsevoi, G.C.B. Alexander, B.W. Wessels, M. G. Kanatzidis, From 0D Cs3Bi2I9 to 2D Cs3Bi2I6Cl3: dimensional expansion induces a direct band gap but enhances electron-phonon coupling, Chem. Mater. 31 (2019) 2644–2650, https://doi.org/10.1021/acs.chemmater.9b00636.
[40] S. Xu, L. Jiang, H. Yang, Y. Song, Y. Dan, Structure and photocatalytic activity of polythiophene/TiO2 composite particles prepared by photoinduced polymerization, Chinese J. Catal. 32 (2011) 536–545, https://doi.org/10.1016/S1872-2067(10)60207-0.

[41] B. Senthilkumar, P. Thenamirtham, R. Kalai Selvan, Structural and electrochemical properties of polythiophene, Appl. Surf. Sci. 257 (2011) 9063–9067. doi:https://doi.org/10.1016/j.apsusc.2011.05.100.
[42] F. Kong, Y. Wang, J. Zhang, H. Xia, B. Zhu, Y. Wang, S. Wang, S. Wu, The preparation and gas sensitivity study of polythiophene/SnO2 composites, Mater. Sci. Eng. B. 150 (2008) 6–11, https://doi.org/10.1016/j.mseb.2008.01.003.
[43] M. Roy, S. Ghorui, J. Bhawna, R. Kangsabanik, A. Yadav, M.A. Alam, Enhanced visible light absorption in layered Cs3Bi2Br 9 halide perovskites: heterovalent Pb2 + substitution-induced defect band formation, J. Phys. Chem. C. 124 (2020) 19484–19491, https://doi.org/10.1021/acs.jpcc.0c05880.
[44] T.R. Dillingham, D.M. Cornelison, S.W. Townsend, Vapor-deposited polythiophene by XPS, Surf. Sci. Spectra. 4 (1996) 142–149, https://doi.org/10.1116/1.1247815.
[45] T. Jiang, W. Malone, Y. Tong, D. Dragoe, A. Bendounan, A. Kara, V.A. Esaulov, Thiophene Derivatives on gold and molecular dissociation processes, J. Phys. Chem. C. 121 (2017) 27923–27935, https://doi.org/10.1021/acs.jpcc.7b08006.
[46] C.J.P. A.V. Naumkin, A. Kraut-Vass, S.W. Gaarenstroom, NIST X-ray Photoelectron Spectroscopy Database 20. Version 4.1, (2012) http://srdata.nist.gov/xps/.
[47] Y. Dai, C. Poidevin, C. Ochoa-Hernández, A.A. Auer, H. Tüysüz, A Supported bismuth halide perovskite photocatalyst for selective aliphatic and aromatic C-H bond activation, Angew. Chemie Int. Ed. 59 (2020) 5788–5796, https://doi.org/10.1002/anie.201915034.
[48] Y. Dai, H. Tüysüz, Rapid acidic media growth of Cs3Bi2Br 9 halide perovskite platelets for photocatalytic toluene oxidation, Sol. RRL. 5 (2021) 2100265, https://doi.org/10.1002/solr.202100265.
[49] X. Zong, X. Miao, S. Hua, L. An, X. Gao, W. Jiang, D. Qu, Z. Zhou, X. Liu, Z. Sun, Structure defects assisted photocatalytic H2 production for polythiophene nanofibers, Appl. Catal. B Environ. 211 (2017) 98–105, https://doi.org/10.1016/j.apcatb.2017.04.033.